The Astrophysical Journal, 836:179 (14pp), 2017 February 20 https://doi.org/10.3847/1538-4357/aa5c37

Modeling the Anomalous Microwave Emission with Spinning Nanoparticles: No PAHs Required

Brandon S. Hensley[1] and B. T. Draine[2]
[1] Jet Propulsion Laboratory, California Institute of Technology, 4800 Oak Grove Drive, Pasadena, CA 91109, USA; brandon.s.hensley@jpl.nasa.gov
[2] Department of Astrophysical Sciences, Princeton University, Princeton, NJ 08544, USA
Received 2016 November 17; revised 2017 January 13; accepted 2017 January 23; published 2017 February 17

Abstract

In light of recent observational results indicating an apparent lack of correlation between the anomalous microwave emission (AME) and mid-infrared emission from polycyclic aromatic hydrocarbons, we assess whether rotational emission from spinning silicate and/or iron nanoparticles could account for the observed AME without violating observational constraints on interstellar abundances, ultraviolet extinction, and infrared emission. By modifying the `SpDust` code to compute the rotational emission from these grains, we find that nanosilicate grains could account for the entirety of the observed AME, whereas iron grains could be responsible for only a fraction, even for extreme assumptions on the amount of interstellar iron concentrated in ultrasmall iron nanoparticles. Given the added complexity of contributions from multiple grain populations to the total spinning dust emission, as well as existing uncertainties due to the poorly constrained grain size, charge, and dipole moment distributions, we discuss generic, carrier-independent predictions of spinning dust theory and observational tests that could help identify the AME carrier(s).

Key words: dust, extinction – radiation mechanisms: general – radio continuum: ISM

1. Introduction

Dust emission encodes information on the composition, size, and temperature of the emitting grains and thus provides a window into the evolution of heavy elements in the interstellar medium (ISM). A notable historical example is the identification of the strong infrared emission features at 3.3, 6.2, 7.7, 8.6, 11.3, 12.0, 12.7, and 13.55 μm with emission from small polycyclic aromatic hydrocarbons (PAHs) transiently heated to very high temperatures (Leger & Puget 1984; Allamandola et al. 1985). PAHs, whose emission is ubiquitous throughout the Milky Way and in external galaxies (Smith et al. 2007), are now thought to constitute roughly 5% of the total Galactic dust mass and account for $\simeq$10% of the interstellar carbon abundance (Allamandola et al. 1989; Draine & Li 2007).

The anomalous microwave emission (AME) is an emission component peaking near 30 GHz, present in both the diffuse ISM and Galactic clouds, that is strongly correlated with the far-infrared (FIR) thermal dust emission (Dobler & Finkbeiner 2008; Planck Collaboration et al. 2014c, 2016c). The AME appears to be emission from interstellar grains and is therefore another observational window into their properties.

Draine & Lazarian (1998a) proposed that the AME is electric dipole radiation from rapidly rotating ultrasmall grains, and this explanation has gained wide acceptance owing to its ability to account for both the observed frequency dependence of the emission (e.g., Draine & Lazarian 1998a; Ysard et al. 2010; Hoang et al. 2011; Planck Collaboration et al. 2014c) and its apparent lack of polarization (Génova-Santos et al. 2015; Planck Collaboration et al. 2016c). In order to be driven to sufficiently high rotation frequencies, the grains must be quite small (radius $a \lesssim 10$ Å), leading to a natural association with the abundant PAHs that give rise to the mid-infrared emission features. Indeed, it has been demonstrated that both the mid-infrared emission features and AME can be simultaneously accounted for by a population of PAHs with reasonable assumptions on their abundance, size distribution, and electric dipole moments (Draine & Lazarian 1998a; Li & Draine 2001).

Recent observations, however, have cast doubt on the association between PAHs and the AME. In the Perseus molecular cloud (Tibbs et al. 2011), the translucent cloud LDN 1780 (Vidal et al. 2011), and the H II region RCW 175 (Tibbs et al. 2012; Battistelli et al. 2015), the spatial morphology of the AME does not match that of PAH emission at 8 and 12 μm. Instead, the AME exhibits stronger correlation with emission from very small grains at 25 and 60 μm, although in these dense regions interpretation is complicated by attenuation of the starlight required to excite the PAH emission. Resolved dust modeling of the nearby spiral galaxy NGC 6946 found a large scatter in the 30 GHz AME intensity per PAH surface density and no clear relationship between the AME strength and the PAH abundance (Hensley et al. 2015). Finally, a full-sky analysis employing *Planck* AME observations and 12 μm *WISE* measurements of PAH emission found no correlation between the strength of the AME and the abundance of PAHs (Hensley et al. 2016).

Spinning dust theory predicts rotational emission from all ultrasmall grains irrespective of composition as long as the grains have an electric or magnetic dipole moment. Given the apparent lack of association between the AME and PAHs, it is natural to ask whether the AME could be spinning dust emission from another carrier. Hensley et al. (2016) suggested spinning nanosilicates as a source for the AME. Hoang et al. (2016) found that spinning nanosilicates can reproduce the AME if their electric dipole moments are sufficiently high. Hoang & Lazarian (2016) found that metallic iron nanoparticles could produce spinning dust emission with a 30 GHz emissivity within a factor of a few of the average Galactic value.

AME has been identified as a significant foreground for upcoming, high-sensitivity CMB experiments aiming to detect primordial B-mode polarization and spectral distortions.

Correct modeling of both the total intensity and polarization of this component is important for unbiased recovery of cosmological parameters (see, e.g., Remazeilles et al. 2016). While we have recently argued that spinning dust emission should be effectively unpolarized owing to quantum mechanical suppression of the grain alignment process (Draine & Hensley 2016), it remains unclear whether the AME is entirely spinning dust emission or whether other emission mechanisms, such as thermal magnetic dipole emission, could be acting in conjunction. A theoretical understanding of the spinning dust spectral energy distribution (SED), as well as its evolution with astrophysical environment, is thus imperative.

The first aim of this work is to assess the viability of silicate and iron nanoparticles as carriers of the AME. In particular, these grains, like the PAHs, undergo stochastic heating and emit in the mid-infrared. We thus ask whether a population of these grains can simultaneously account for the AME without producing more infrared emission than is observed. Likewise, we assess whether such grains would produce more ultraviolet extinction than is observed. We find that nanosilicates can reproduce the observed AME without violating observational constraints, whereas iron nanoparticles cannot. The second aim of this work is to describe the observational predictions of spinning dust theory that are carrier independent. Within this more generic framework, we suggest observational tests that would help determine whether emission from spinning grains accounts for part or the entirety of the observed AME.

This paper is organized as follows. In Section 2, we specify the material properties of the silicate and iron nanoparticles under assessment. In Section 3, we compute the spinning dust emission from populations of silicate and iron nanoparticles for various assumptions on their size distribution. In Sections 4 and 5, we compute the infrared emission and ultraviolet extinction, respectively, from these grains and compare to observational data. In Section 6, we discuss carrier-independent predictions of spinning dust emission and observational tests for identifying the AME with a specific carrier. In Section 7, we describe the implications of our results for the viability of non-PAH nanoparticles as carriers of the AME. We summarize our conclusions in Section 8.

2. Potential Carriers

2.1. Silicate Grains

Silicon is highly depleted in the gas phase (e.g., Jenkins 2009), and amorphous silicate grains have been robustly identified as a major component of interstellar dust on the basis of strong extinction features at 9.7 and 18 μm. A significant population of sub-nanometer silicate grains is a plausible component of the interstellar dust.

In this work, we assume that silicate grains have a chemical composition of $Mg_{1.48}Fe_{0.32}SiO_{3.79}$ and a mass density of 3.4 g cm^{-3} (Poteet et al. 2015; Hensley & Draine 2017). We adopt an interstellar solid-phase silicon abundance of 40 ppm in accord with protostellar abundances and chemical enrichment (Chiappini et al. 2003; Asplund et al. 2009) with 96% of the Si depleted onto dust (Jenkins 2009) and define $Y_{\rm Si}$ as the fraction of the solid-phase interstellar silicon in nanosilicate grains. We adopt the dielectric function for amorphous silicate of Hensley & Draine (2017) and compute the grain temperature distributions following the methods of Draine & Li (2001).

As has been done with PAHs by previous studies, we model the electric dipole moment of an amorphous silicate grain as the result of a random walk such that the rms electric dipole moment scales as $\sqrt{N_{\rm at}}$, where $N_{\rm at}$ is the number of atoms in the grain, given by

$$N_{\rm at} \simeq 395\left(\frac{a}{10\ \text{Å}}\right)^3. \quad (1)$$

Thus, the probability of a grain of $N_{\rm at}$ atoms having an intrinsic electric dipole moment μ_i is given by

$$dP(\mu_i) \propto \mu_i^2 e^{-3\mu_i^2/(2\beta^2 N_{\rm at})}\, d\mu_i, \quad (2)$$

where β is the rms dipole moment per atom.

In addition to the intrinsic dipole moment, we also consider a dipole moment arising from the displacement of the grain's charge centroid from its center of mass. Following Draine & Lazarian (1998b), we take the magnitude of this electric dipole moment to be $\epsilon a_x Ze$, where Ze is the grain charge and ϵa_x is the vector displacement between the charge centroid and the center of mass. We adopt $\epsilon = 0.01$ and, for the spherical grains considered in this work, $a = a_x$ (note that disk-like grains such as small PAHs have a_x given by Equation (3) of Draine & Lazarian 1998b). Thus, the total electric dipole moment is

$$\mu^2 = \mu_i^2 + (\epsilon a_x Ze)^2. \quad (3)$$

If the electric dipole moment and rotation axis are randomly oriented, as might be expected in spherical grains, then the component of μ along the rotation axis has an average magnitude of $\mu_\perp^2 = 2\mu^2/3$. To compute the spinning dust emissivity from a population of grains with $N_{\rm at}$ atoms, we average Equation (3) over the μ_i distribution of Equation (2) following Ali-Haïmoud et al. (2009). In this work we consider $\beta = 0.3$ and 1.0 D, with the former value corresponding roughly to the value adopted for PAHs and the latter an estimate based on various silicate materials (see Hoang et al. 2016, Table 1).

2.2. Iron Grains

Like silicon, iron is heavily depleted in the gas phase (e.g., Jenkins 2009) and is thus a major constituent of interstellar dust. The presence of included iron nanoparticles in lunar soil grains (Keller & McKay 1997), interplanetary dust particles (Bradley 1994), and putative interstellar grains found in the solar system (Westphal et al. 2014; Altobelli et al. 2016) suggests that iron nanoparticles could be a significant constituent of interstellar dust.

In this work, we consider populations of iron nanoparticles with mass density $\rho = 7.87$ g cm^{-3}. We adopt an interstellar iron abundance of 41 ppm in accord with observations of young F and G stars (Bensby et al. 2005; Lodders et al. 2009), with 99% of the interstellar iron depleted onto grains (Jenkins 2009). We define $Y_{\rm Fe}$ as the fraction of the solid-phase iron present in the form of iron nanoparticles and adopt the metallic iron dielectric function of Draine & Hensley (2013).

2.2.1. Magnetic Dipole Moment of Fe Nanoparticles

Because metallic Fe is conductive, the electric dipole moment is expected to be small for pure Fe nanoparticles. However, unlike nanosilicates and PAHs, metallic iron nanoparticles are ferromagnetic and can produce spinning dust emission due to their *magnetic* dipole moment μ_m (Hoang &

Lazarian 2016). The magnetization is ordered, and therefore the total magnetic dipole moment grows linearly with the number of iron atoms, in contrast to the random walk process used to model the total electric dipole moments of nanosilicates and PAHs. We therefore adopt

$$\mu_m = 0.027 N_{\rm at}\ {\rm D}, \tag{4}$$

where we have assumed a magnetic dipole moment per atom of $3\mu_{\rm B}$, appropriate for small clusters of iron atoms ($N_{\rm at} \lesssim 200$; Billas et al. 1993; Tiago et al. 2006). For metallic iron grains,

$$N_{\rm at} \simeq 352\left(\frac{a}{10\ {\rm Å}}\right)^3. \tag{5}$$

For these grains we also consider the small electric dipole moment that could arise from the displacement of the grain's charge centroid from its center of mass. We assume that this dipole moment and the magnetic dipole moment are oriented randomly, thus giving the grain a total dipole moment of

$$\mu^2 = \mu_m^2 + (\epsilon a_x Z e)^2, \tag{6}$$

where we adopt $\epsilon = 0.01$ and $a_x = a$ as for the silicate grains. For a grain with $Z = 1$ and $a = 4.5$ Å, the electric dipole moment due to the charge distribution (proportional to Za) is a factor of four smaller than its magnetic moment (proportional to a^3). Thus, the electric dipole moment due to the grain charge distribution is a small correction for all grain sizes of interest.

2.2.2. Electric Dipole Moment of Impure Fe Nanoparticles

While pure quasi-spherical iron nanoparticles seem unlikely to have electric dipole moments even if charged, there may be nanoparticles that are predominantly Fe but that also contain non-Fe atoms, such as C or O. If these are distributed more or less randomly, it is plausible that the predominantly Fe nanoparticle could have an electric dipole moment of several debye.

To explore this effect, we also compute the rotational emission from a population of iron grains assuming that a grain of $N_{\rm at}$ atoms has an rms electric dipole moment of $\beta\sqrt{N_{\rm at}}$, as we assumed for silicate grains, in addition to its magnetic dipole moment and electric dipole moment due to its charge distribution. Thus,

$$\mu^2 = \mu_m^2 + \mu_i^2 + (\epsilon a_x Z q_e)^2, \tag{7}$$

where we average the electric dipole moment μ_i over the distribution given by Equation (2) and adopt $\beta = 0.3$ D.

2.3. Size Distribution

Following previous studies modeling spinning dust emission (e.g., Draine & Lazarian 1998a; Hoang et al. 2016), we consider a lognormal grain size distribution with

$$\frac{1}{n_{\rm H}}\frac{dn}{da} = \frac{B}{a}\exp\left\{-\frac{1}{2}\left[\frac{\ln(a/a_0)}{\sigma}\right]^2\right\}, \tag{8}$$

where the parameters a_0 and σ determine the peak size and width of the size distribution. B is a normalization constant given by

$$B = \frac{3}{(2\pi)^{3/2}}\frac{\exp(-4.5\sigma^2)}{a_0^3\rho\sigma} \times \frac{m_{\rm X} b_{\rm X}}{1 + {\rm erf}\left[3\sigma/\sqrt{2} + \ln(a_0/a_{\rm min})/\sigma\sqrt{2}\right]} \tag{9}$$

for $a > a_{\rm min}$ and 0 otherwise, where ρ is the grain mass density, $m_{\rm X}$ is the grain mass per atom of element X, and $b_{\rm X}$ is the number of X atoms per H consumed by this grain population.

The very smallest grains are subject to rapid sublimation by the interstellar radiation field. Guhathakurta & Draine (1989) found that silicate grains of fewer than 37 atoms ($a \lesssim 4.5$ Å) are photolytically unstable in the local interstellar radiation field (assuming the spectrum of Mathis et al. 1983), and thus we truncate the silicate grain size distribution at $a_{\rm min} = 4.5$ Å. Likewise, Hensley & Draine (2017) found that iron grains could persist down to a radius of 4.5 Å, and so we adopt $a_{\rm min} = 4.5$ Å for the metallic iron grains as well.

3. Spinning Dust Emissivity

In this section, we assess whether the observed AME can be reproduced by spinning nanosilicate or iron grains.

3.1. Methodology

To compute the spinning dust emission from ultrasmall silicate and iron grains, we employ the `SpDust` code (Ali-Haïmoud et al. 2009; Silsbee et al. 2011). As the code is optimized for PAHs, several important changes were necessary.

First, we have assumed that all silicate and iron grains are spherical rather than having a population of disk-like grains below some radius. We note that irregular grains can have slightly higher emissivities and peak frequencies than spherical grains of equal mass (Hoang et al. 2011).

Second, we have employed the formalism of Weingartner & Draine (2001b) and Hensley & Draine (2017) to compute the charge distributions of small silicate and iron grains, respectively. We have made a small change to the charging calculations of PAHs and silicates by adopting the functional form of $E_{\rm min}$ (the minimum energy at which an electron is capable of tunneling out of a grain) suggested by van Hoof et al. (2004, Equation (1)) (cf. Weingartner & Draine 2001b, Equation (7)).

Third, we have calculated the temperature distributions and resulting infrared emission of both silicate and iron grains following the methods of Draine & Li (2001) in order to compute the rotational damping and excitation due to infrared emission.

Fourth, Ali-Haïmoud et al. (2009) computed the temperature $T_{\rm ev}$ of atoms evaporating from the surface of PAHs taking into account the ejection of adsorbed atoms during stochastic heating events. In this work, we adopt their $T_{\rm ev}$ as a function of grain size and radiation field intensity for all grains irrespective of composition. However, unlike Ali-Haïmoud et al. (2009), we assume that we are always in the limit that there are available sites on the grain for atoms to stick (see their Equation (60)).

Fifth, the rotational velocity distribution of spinning grains depends in part on the ability of the grain to rotationally couple

Table 1
Idealized ISM Phases

Parameter	CNM	WNM	WIM	RN	PDR
$n_{\rm H}\,({\rm cm}^{-3})$	30	0.4	0.1	10^3	10^5
$T_g\,({\rm K})$	100	6000	8000	100	300
χ	1	1	1	1000	3000
$x_{\rm H} \equiv n({\rm H}^+)/n_{\rm H}$	0.0012	0.1	0.99	0.001	0.0001
$x_{\rm C} \equiv n({\rm C}^+)/n_{\rm H}$	0.0003	0.0003	0.001	0.0002	0.0002
$y \equiv 2n({\rm H}_2)/n_{\rm H}$	0	0	0	0.5	0.5
γ	0	0	0	0.1	0.1

Note. Parameters for the idealized ISM models of Draine & Lazarian (1998b): hydrogen number density $n_{\rm H}$, gas temperature T_g, radiation intensity parameter χ, H^+ abundance $x_{\rm H}$, C^+ abundance $x_{\rm C}$, H_2 abundance y, and H_2 formation efficiency γ. Grains are assumed to be illuminated by a radiation field with spectrum given by Mathis et al. (1983) multiplied by a frequency-independent factor χ.

to distant plasma via its dipole moment. However, this coupling is much stronger to a grain's electric dipole moment than to its magnetic dipole moment. Thus, when computing the effects of plasma drag, we consider the magnitude of the grain's electric dipole moment only. Likewise, we ignore the effect of the grain's magnetic dipole moment on the trajectory of colliding ions (see Ali-Haïmoud et al. 2009, Equations (90) and (91)).

Finally, we have updated the relevant parts of the code with the material properties of silicate and iron (e.g., mass density, number of atoms per grain mass, index of refraction, etc.).

We investigate the spinning dust emission in a variety of interstellar environments—the cold neutral medium (CNM), warm neutral medium (WNM), warm ionized medium (WIM), reflection nebulae (RNs), and photodissociation regions (PDRs). We adopt the idealized physical parameters of these environments proposed by Draine & Lazarian (1998a), which we list in Table 1.

3.2. Comparison to Other Studies

Our calculations of the emission from spinning silicate and iron nanoparticles are in many ways complementary to those of Hoang et al. (2016) and Hoang & Lazarian (2016), respectively, as they are based on somewhat different approaches and assumptions.

First, by using the `SpDust` code, we are employing the Fokker–Planck equation to compute the rotational velocity distribution of small grains. In contrast, the aforementioned studies employ an approach based on the Langevin equation that was modified in order to incorporate the effects of stochastic impulsive torques. However, Hoang et al. (2010) found that impulsive events had only a minor effect, slightly raising the peak frequency and slightly extending the high-frequency tail of the emission spectrum. Hence, our Fokker–Planck treatment is a good approximation.

Second, Hoang et al. (2011) demonstrated that the spinning dust spectrum of PAHs averaged over a realistic temperature distribution was nearly identical to one in which the dust temperature was fixed to 60 K. Thus, Hoang et al. (2016) adopt $T_d = 60$ K for silicate grains, while Hoang & Lazarian (2016) compute spinning dust spectra of iron grains with $T_d = 20$ and 40 K. In contrast, we solve for the full temperature distribution and resultant infrared emission from these grains, which affects the magnitude of the infrared damping. For a 1 nm silicate grain, Hoang et al. (2016) find IR damping and excitation coefficients of $F_{\rm IR} = 0.6$ and $G_{\rm IR} = 0.7$, respectively. In contrast, we find $F_{\rm IR} = 3.0$ and $G_{\rm IR} = 0.7$.

Third, those studies adopted $a_{\rm min} = 3.5$ Å, i.e., the same as PAHs, whereas we employ $a_{\rm min} = 4.5$ Å based on the sublimation rates for silicate and iron grains (Guhathakurta & Draine 1989; Hensley & Draine 2017).

Finally, unlike Hoang et al. (2016) and Hoang & Lazarian (2016), we do not employ observational constraints based on polarization. We have recently argued that the alignment of ultrasmall grains is dramatically reduced owing to quantum suppression of the conversion of rotational to vibration energy (Draine & Hensley 2016). Insofar as this is the case, all emission from ultrasmall nanoparticles will be unpolarized, and thus the lack of observed AME polarization provides no additional constraints on the properties of the emitting grains. While it remains possible that this suppression can be overcome by other mechanisms such as spin-lattice relaxation or anisotropic starlight, this has yet to be demonstrated. Therefore, instead of employing polarization constraints, we calculate the infrared emission and ultraviolet extinction from populations of nanosilicate and iron grains that could account for the observed AME and then compare to observations. Nevertheless, as we demonstrate below, our conclusions reached regarding the AME emissivity of iron and silicate nanoparticles are qualitatively similar to those of Hoang et al. (2016) and Hoang & Lazarian (2016).

3.3. Results

In the top panels of Figure 1, we compare the spinning dust power per grain as a function of grain size for PAHs, nanosilicates, and iron nanoparticles in the CNM, WNM, and WIM interstellar environments of Table 1. It is evident that spinning dust emission is strongly sensitive to the grain size distribution and, in particular, the abundance of the very smallest grains.

In the bottom panels of Figure 1, we compare the peak frequency of the spinning dust emissivity j_ν of each grain size for each interstellar environment. Again, strong dependence on grain size is observed.

Given the strong dependencies on grain size, we consider several grain size distributions for each grain material, which we summarize in Table 2. In brief, we adopt $a_0 \in \{a_{\rm min}, 6\,{\rm Å}\}$ and $\sigma \in \{0.1, 0.3\}$. We plot the resulting spinning dust spectrum for each size distribution in Figure 2, where we have set $Y_{\rm Si}$ and $Y_{\rm Fe}$ to 1.0 to obtain a maximum total emissivity for each combination of composition and size distribution.

We note that the emissivities obtained for populations of silicate and iron nanoparticles are similar (within a factor of a few) to those derived by Hoang et al. (2016) and Hoang & Lazarian (2016), respectively, when employing the same size distribution and value of Y. However, when adopting the more physically motivated minimum grain size of $a_{\rm min} = 4.5$ Å (instead of 3.5 Å, the same as for PAHs), we derive somewhat lower emissivities. Indeed, for models of silicate grains with $\beta = 0.3$ D in CNM conditions and $\sigma = 0.1$, we find a factor of two increase in 30 GHz emissivity when adopting $a_0 = a_{\rm min} = 3.5$ Å versus 4.5 Å. Likewise, the small changes in the grain size distribution represented by models 1–4 differ by roughly an order of magnitude in peak emissivity. This

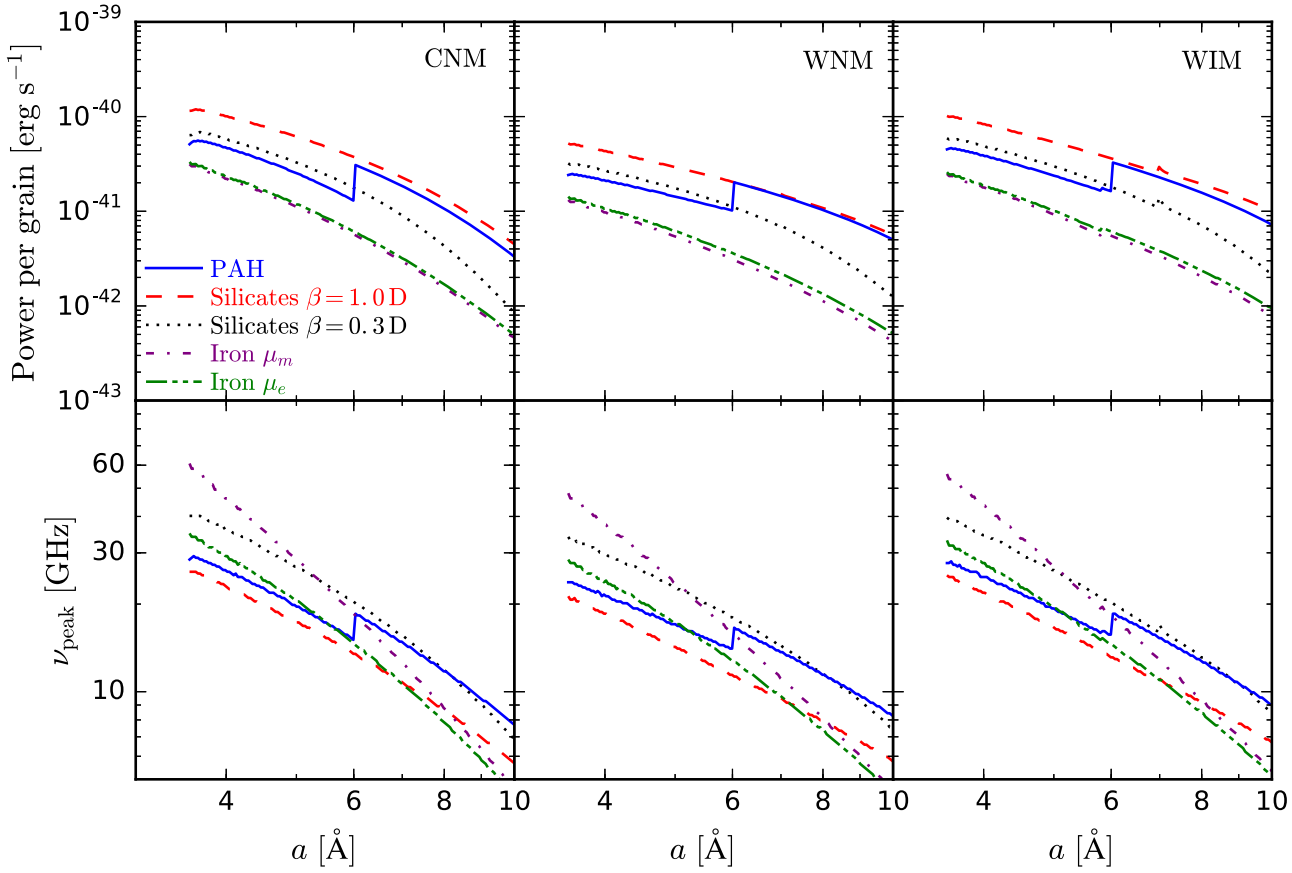

Figure 1. Top panels: comparison of the rotational power emitted per grain as a function of grain size for PAHs, nanosilicates, and iron nanoparticles in CNM (left), WNM (middle), and WIM (right) conditions. Bottom panels: comparison of the peak frequency of the spinning dust emissivity j_ν as a function of grain size for PAHs, nanosilicates, and iron nanoparticles in CNM (left), WNM (middle), and WIM (right) conditions. We use "μ_m" and "μ_e" to denote pure iron nanoparticles with a total dipole moment given by Equation (6) and impure iron nanoparticles with a total dipole moment given by Equation (7), respectively.

Table 2
Grain Size Distributions

Model Number	a_0 (Å)	σ	$Y^{\rm min}_{\rm Si,1.0}$	$Y^{\rm min}_{\rm Si,0.3}$	$Y^{\rm max}_{\rm Si}$	$Y^{\rm min}_{{\rm Fe},\mu_m}$	$Y^{\rm min}_{{\rm Fe},\mu_e}$	$Y^{\rm max}_{\rm Fe}$
1	$a_{\rm min}$	0.1	0.17	0.04	0.21	0.63	1.18	0.46
2	$a_{\rm min}$	0.3	0.73	0.14	0.15	2.38	5.67	0.34
3	6.0	0.1	2.51	0.25	0.13	6.40	39.3	0.30
4	6.0	0.3	2.50	0.42	0.18	7.69	21.1	0.38

Note. Parameters for the grain size distributions of models considered in this work. We adopt $a_{\rm min} = 4.5$ Å for both silicate and iron grains. We determine $Y^{\rm min}$ by requiring the 30 GHz spinning dust emissivity of that size distribution to be 3×10^{-18} Jy sr^{-1} cm^2 H^{-1} for CNM conditions. $Y^{\rm min}_{\rm Si,1.0}$ and $Y^{\rm min}_{\rm Si,0.3}$ denote $Y^{\rm min}$ for nanosilicate grains with $\beta = 1.0$ and 0.3 D, respectively. $Y^{\rm min}_{{\rm Fe},\mu_m}$ and $Y^{\rm min}_{{\rm Fe},\mu_e}$ denote $Y^{\rm min}$ for pure iron nanoparticles with a total dipole moment given by Equation (6) and impure iron nanoparticles with a total dipole moment given by Equation (7), respectively. We determine $Y^{\rm max}$ by requiring the mid-infrared emission from grains with the specified size distribution to reproduce the observed 10 μm emission for silicates and the 25 μm emission for iron grains.

further underscores the sensitivity of the spinning dust emissivity to the abundance of the smallest grains.

The Galactic AME has an observed emissivity of roughly 3×10^{-18} Jy sr^{-1} cm^2 H^{-1} at 30 GHz in both Galactic clouds and the diffuse ISM (Dobler et al. 2009; Tibbs et al. 2010, 2011; Planck Collaboration et al. 2014b, 2014c), and we therefore consider models viable only if they can reproduce this emissivity. However, observations of AME in the diffuse ISM suggest that the emission may be peaking closer to 20 GHz (Miville-Deschênes et al. 2008; Planck Collaboration et al. 2016a). In Figure 3, we illustrate the range of fit AME SEDs from the *Planck* `Commander` analysis (Planck Collaboration et al. 2016a), demonstrating that the 20 GHz specific intensity is on average ≃20%–30% higher than the 30 GHz specific intensity. Therefore, while successful models still need to reproduce the observed 3×10^{-18} Jy sr^{-1} cm^2 H^{-1} at 30 GHz, those that peak at lower frequencies may be favored. For all models, we define $Y^{\rm min}$ as the minimum value of Y such that the model has a 30 GHz emissivity of 3×10^{-18} Jy sr^{-1} cm^2 H^{-1}.

From Figure 2, it is clear that nanosilicate grains are able to produce considerable rotational emission and may account for the entirety of the AME. The SEDs for models 1 and 2, which

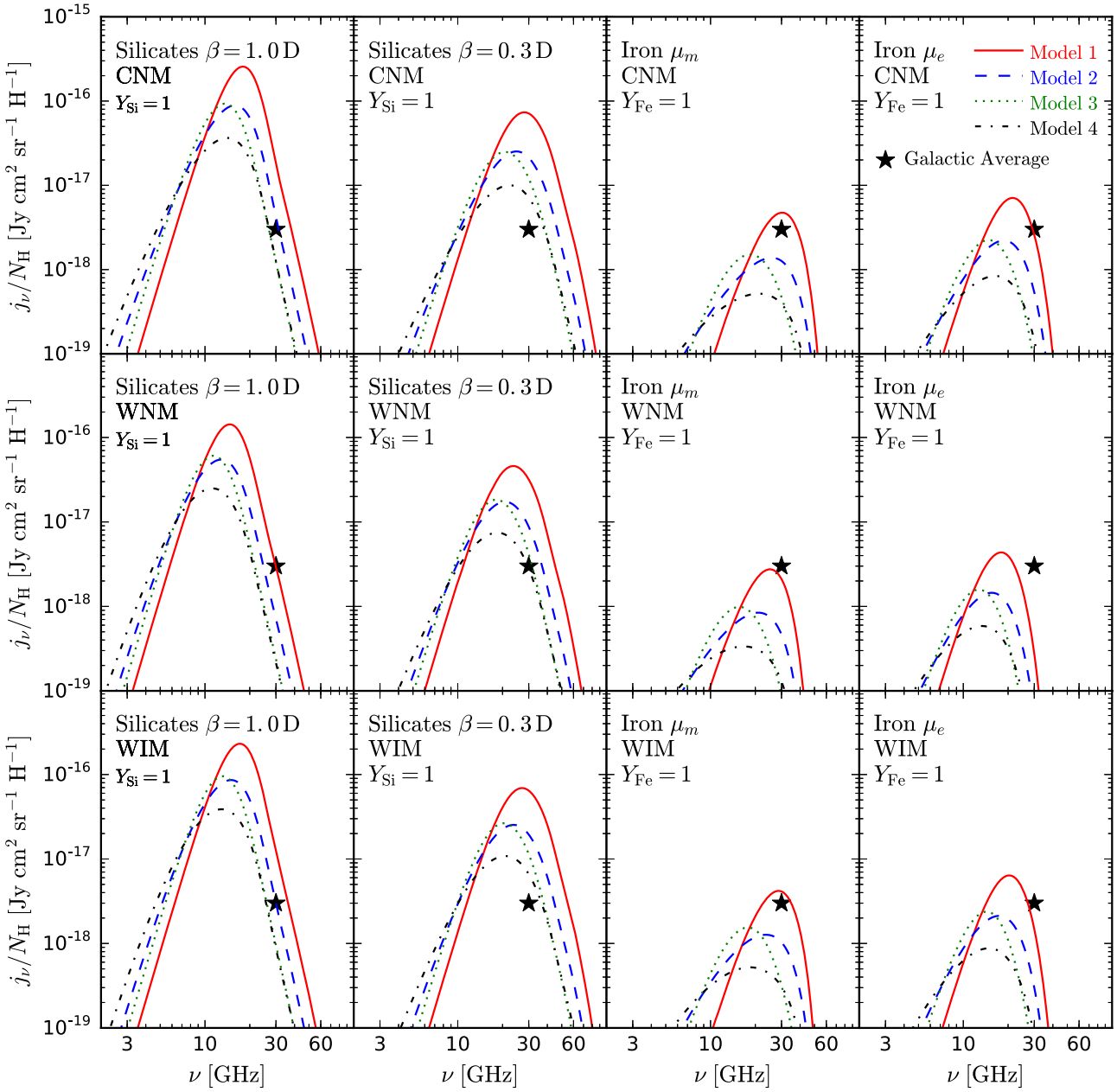

Figure 2. Spinning dust SEDs of nanosilicates with $\beta = 1.0$ D (first column), nanosilicates with $\beta = 0.3$ D (second column), pure iron nanoparticles with a total dipole moment given my Equation (6) (third column), and impure iron nanoparticles with a total dipole moment given by Equation (7) (fourth column) for the size distributions defined in Table 2 with $Y = 1.0$ and for CNM, WNM, and WIM environments. The observed Galactic spinning dust emissivity at 30 GHz is approximately 3×10^{-18} Jy sr^{-1} cm^2 H^{-1} and is indicated by a star. Several models of nanosilicate grains (model 1 for $\beta = 1.0$ D and models 1 and 2 for $\beta = 0.3$ D) can account for the entirety of the AME signal with $Y_{Si} < 20\%$. In contrast, for pure iron, only the model concentrating most of the interstellar iron in the smallest nanoparticles (model 1) is able to produce a comparable amount of AME, but it consumes nearly two-thirds of the interstellar iron. All models of impure iron grains with an appreciable electric dipole moment produce insufficient 30 GHz emission.

concentrate most of the grain mass into the smallest nanoparticles, and $\beta = 0.3$ D both peak near 30 GHz and can approximately reproduce the observed AME spectrum with $Y_{Si} = 0.04$ or 0.14, respectively. Models with $\beta = 1.0$ D peak at lower frequencies owing to the enhanced damping from electric dipole emission. While model 1 with $\beta = 1.0$ D can reproduce the observed AME emissivity while consuming only a modest amount of the interstellar silicon ($Y_{Si} = 0.17$), the remaining $\beta = 1.0$ D models produce inadequate 30 GHz emission.

In contrast, iron nanoparticles are able to reproduce the observed 30 GHz AME without overconsuming the available iron only for pure iron grains with the size distribution that concentrates the grain mass in the very smallest grains, although even this size distribution consumes roughly two-thirds of the available iron ($Y_{Fe} = 0.63$). Iron grains may, however, be contributing a portion of the AME signal particularly at ~20 GHz.

The discrepancy in emissivity between the nanosilicate and iron grains arises for several reasons. First, the iron grains are much denser, giving them a larger moment of inertia than silicate grains of the same radius. Second, the abundances of solid-phase Si and Fe in the ISM are roughly equal. However, silicate grains are a mix of Si, O, Mg, and Fe, whereas metallic iron grains are pure Fe. Thus, the number of nanoparticles is

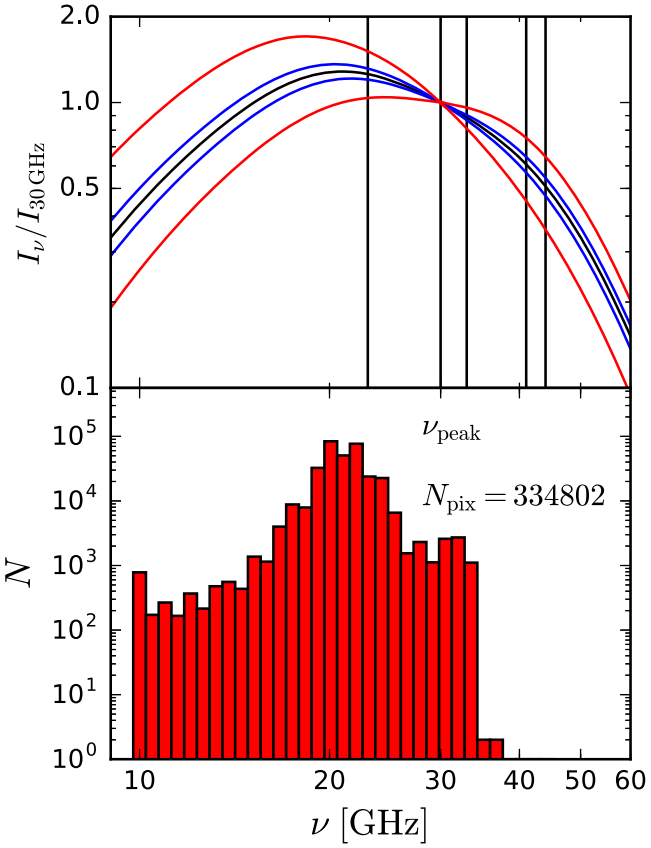

Figure 3. Given the full-sky fits to the AME performed by Planck Collaboration et al. (2016a), in the top panel we plot the median (black), 68% confidence interval (blue), and 95% confidence interval (red) of the AME SEDs normalizing to 1 at 30 GHz. We note that we have masked the Galactic plane within $|b| < 5°$, as well as pixels in which the fit AME amplitude was less than five times the quoted fit uncertainty. This leaves 334,802 pixels at $N_{\mathrm{side}} = 256$, about 43% of the sky. The vertical lines indicate the 23, 33, and 41 GHz *WMAP* bands and the 30 and 44 GHz *Planck* bands. In the bottom panel, we plot the histogram of AME peak frequencies in these pixels.

much greater in models with $Y_{\mathrm{Si}} = 1$ than in models with $Y_{\mathrm{Fe}} = 1$.

4. Infrared Emission

Both silicate and iron nanoparticles undergo stochastic heating and emit at mid-infrared wavelengths. In this section, we place limits on the abundance of silicate and iron nanoparticles based on the latest observational constraints on the mid-infrared emission of the diffuse ISM. Although the wavelengths under consideration are much larger than the relevant grain sizes, the infrared emission retains sensitivity to the size distribution owing to the size dependence of the transient heating of small grains.

Nanosilicate grains have a strong mid-infrared signature due to emission in the 9.7 μm feature. Li & Draine (2001) found that at most 15% of interstellar silicon could be in dust with $a < 10$ Å on the basis of a 4.5–11.7 μm spectrum of the diffuse ISM taken by the Infrared Telescope in Space (Onaka et al. 1996).

More recent spectroscopic observations from *Spitzer* and *AKARI* allow us to place new constraints tailored to grain populations capable of reproducing the AME. Ingalls et al. (2011) employed the *Spitzer* Infrared Spectrograph to obtain a 5.2–38 μm spectrum of the translucent cloud DCld 300.2-16.9,

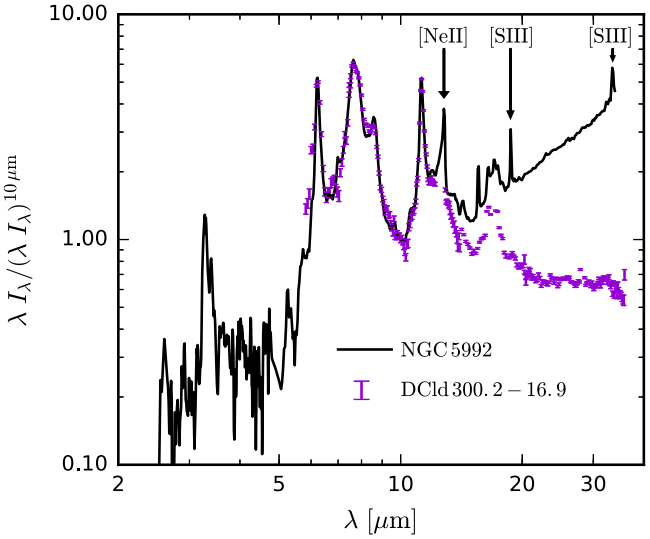

Figure 4. Comparison of the mid-infrared spectra of NGC 5992 (Brown et al. 2014) after starlight subtraction (black solid line) and the Galactic translucent cloud DCld 300.2-16.9 (Ingalls et al. 2011; violet data points). Both spectra have been normalized to 1 at 10 μm. Given the excellent concordance of the two spectral shapes, we employ the combined 3–12 μm spectrum as a constraint on the mid-infrared dust emission from ultrasmall grains.

which we adopt to typify the diffuse ISM. In order to extend the observed spectrum to shorter wavelengths, we also employ the combined *AKARI* and *Spitzer* spectrum of the star-forming SBb galaxy NGC 5992 compiled by Brown et al. (2014). To remove the starlight component, we have subtracted a 5000 K blackbody from this spectrum. Due to the uncertainty associated with this subtraction, we do not employ the starlight-subtracted spectrum at wavelengths shorter than 3 μm.

The shapes of these two spectra are in excellent agreement in the range $\simeq$5–12 μm (Figure 4), diverging at longer wavelengths presumably because the starlight in NGC 5992 is more intense, resulting in higher temperatures for the big grains. In addition, the NGC 5992 spectrum includes line emission from H II regions, in particular [Ne II] 12.81 μm and [S III] 18.71 μm, that are of course absent from the DCld 300.2-16.9 spectrum. We scale this spectrum to match the H I-correlated dust emission in the mid-infrared DIRBE bands as measured by Dwek et al. (1997). Since the spectrum of NGC 5992 extends to shorter wavelengths and the spectrum of DCld 300.2-16.9 better matches the shape of the DIRBE SED, we employ the former as a constraint between 3 and 12 μm and the latter longward of 12 μm.

We compute the emission from silicate and iron grains by solving for the temperature distribution function at each grain radius a following Draine & Li (2001). Given that DIRBE measured dust emission from diffuse, high-latitude regions, we assume that the grains are illuminated by a radiation field $10^{0.2} \simeq 1.6$ times as intense as the standard Mathis et al. (1983) radiation field. This scaling factor can be derived from the FIR dust radiance measured by *IRAS* and *Planck* (Planck Collaboration et al. 2014a) and a standard $R_V = 3.1$ extinction curve (e.g., Fitzpatrick & Massa 2007) using the fact that power absorbed must equal power radiated and assuming a dust albedo of $\simeq$0.4 at optical–UV wavelengths.

In Figure 5, we compare the observed mid-infrared SED to emission from nanosilicates and iron nanoparticles, where we have set Y_{Si} and Y_{Fe} to their minimum values (as given in Table 2) required to reproduce the entirety of the Galactic AME

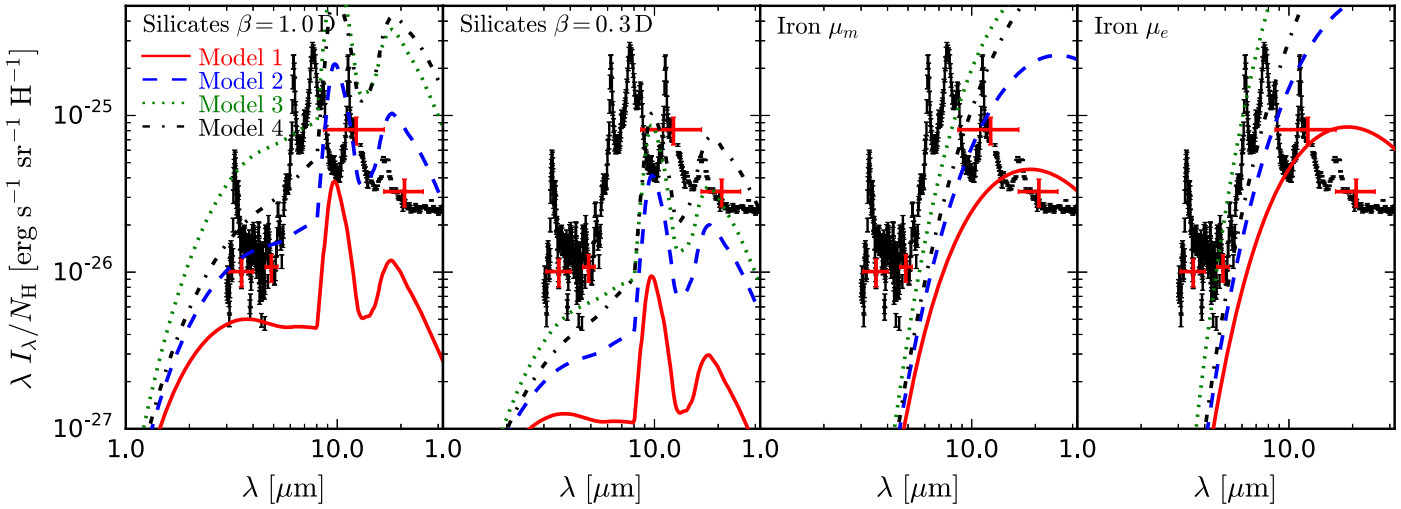

Figure 5. In each panel, we plot the combined MIR spectrum of NGC 5992 (Brown et al. 2014) and DCld 300.2-16.9 (Ingalls et al. 2011) in black, which has been scaled to match the H I-correlated high-latitude dust emission observed by DIRBE (Dwek et al. 1997; red error bars). In the first panel, we plot the SEDs of silicate grains with $\beta = 1.0$ D and size distributions given by Table 2 and with $Y_{\rm Si} = Y_{\rm Si,1.0}^{\rm min}$. In the second panel, we plot the same for silicate grains with $\beta = 0.3$ D and $Y_{\rm Si} = Y_{\rm Si,0.3}^{\rm min}$. In the third and fourth panels, we plot the same for pure iron nanoparticles and impure iron nanoparticles with an appreciable electric dipole moment having $Y_{\rm Fe} = Y_{{\rm Fe},\mu_m}^{\rm min}$ and $Y_{\rm Fe} = Y_{{\rm Fe},\mu_e}^{\rm min}$, respectively. Silicate grains could produce the entirety of the AME without violating observed abundances or mid-infrared emission for either value of β and the model 1 size distribution, whereas all models with a sufficient number of iron nanoparticles to account for the observed AME produce more $\simeq$20 μm emission than is observed.

at 30 GHz. We define $Y_{\rm Si}^{\rm max}$ as the value of $Y_{\rm Si}$ at which the nanosilicates reproduce all of the observed 10 μm emission, while we define $Y_{\rm Fe}^{\rm max}$ as the value of $Y_{\rm Fe}$ at which the iron nanoparticles reproduce all of the observed emission in the 25 μm DIRBE band. These values are listed in Table 2.

Silicate grains can simultaneously reproduce the observed 30 GHz AME emissivity while respecting the constraints on infrared emission only for the size distributions concentrating the grain mass into the smallest nanoparticles (models 1 and 2). In particular, model 1 silicate grains with $\beta = 0.3$ D and $Y_{\rm Si} = Y^{\rm min}$ make only a small contribution to the infrared emission. In contrast, none of the models of rotational magnetic dipole emission from iron nanoparticles can account for all of the AME while respecting constraints on the observed infrared emission. We thus conclude that if there is a population of iron nanoparticles in the ISM, their rotational emission constitutes only a fraction of the observed AME.

An example nanosilicate model that would be compatible with the median AME peak frequency of $\simeq$22 GHz and the observed AME emissivity for CNM conditions has a model 1 size distribution with $Y_{\rm Si} = 0.06$ and electric dipole moments given by Equation (3), with 65% of the grains having $\beta = 0.2$ D and the remaining 35% having $\beta = 0.7$ D. The top panel of Figure 6 shows the microwave emission from this population. For comparison, we also show the 68% confidence interval of the AME spectrum inferred by Planck Collaboration et al. (2016a) (see Figure 3). Note that the AME SED inferred by *Planck* is really only constrained at 23, 30, 33, 41, and 44 GHz, the frequencies where *WMAP* and *Planck* observations were made.

The infrared emission for this example is shown in the bottom panel of Figure 6 and falls well below the observational constraints. We emphasize that the model in Figure 6 is only presented as an example where the nanosilicates account for all of the AME. In reality, it seems likely that several nanoparticle components (silicates, PAHs, Fe) will each account for a fraction of the AME.

5. Ultraviolet Extinction

A second constraint on the abundance of interstellar nanoparticles is the ultraviolet extinction. Fitzpatrick & Massa (2007) derived a mean Galactic extinction curve from UV to IR wavelengths based on a sample of 243 stars. To normalize the extinction to the hydrogen column, we take $N_{\rm H}/E(B-V) = 7.7 \times 10^{21}$ cm^{-2} mag^{-1}, consistent with studies based on recent high-latitude H I surveys and reddening maps (Liszt 2014a, 2014b; Planck Collaboration et al. 2016b). We plot this curve in Figure 7 and adopt it as our benchmark.

Draine & Hensley (2013) demonstrated that 100% of the interstellar iron could be in the form of $a = 5$ nm Fe nanoparticles without making a significant contribution to the interstellar extinction (see their Figure 11). As optical–UV wavelengths are much larger than the grain sizes of relevance for spinning dust emission (i.e., the Rayleigh limit), the total extinction will be insensitive to the nanoparticle size distribution. Thus, we conclude that the UV extinction provides no additional constraints on the abundance of iron nanoparticles than were derived in Section 4.

Li & Draine (2001) considered the contributions of ultrasmall silicate grains to the UV extinction curve by adding additional ultrasmall silicate grains to the dust model of Weingartner & Draine (2001a). They found that models that included an additional $\Delta Y_{\rm Si} \gtrsim 0.20$ of ultrasmall silicate grains exceeded the observed extinction at $\lambda^{-1} \gtrsim 7$ μm^{-1}.

In Figure 7, we plot the total extinction from a population of silicate nanoparticles with $Y_{\rm Si} = 1$. At the shortest wavelengths with observational data, the ultrasmall silicates can only contribute about two-thirds of the total extinction. Without self-consistently modeling contributions from larger silicate grains, as well as grains of other compositions, it is not possible to derive more stringent limits on the amount of silicon in nanoparticles than the $Y_{\rm Si}^{\rm max}$ derived in Section 4 on the basis of infrared emission.

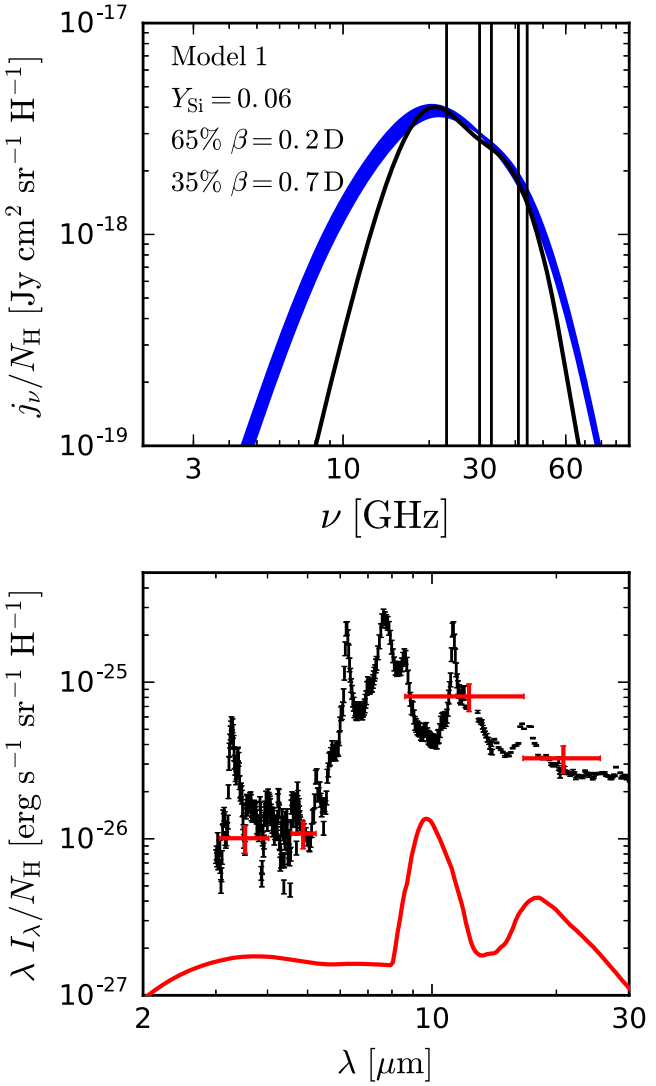

Figure 6. Top: 68% confidence interval of the normalized `Commander` AME SEDs, which here we normalize to 3×10^{-18} Jy sr^{-1} cm^2 H^{-1} at 30 GHz (blue shaded region). We also plot a model of nanosilicate grains having a model 1 size distribution with $Y_{Si} = 0.06$, 65% of the grains having an electric dipole moment given by Equation (3) and $\beta = 0.2$ D, and 35% of the grains having $\beta = 0.7$ D. The vertical lines indicate the 23, 33, and 41 GHz *WMAP* bands and the 30 and 44 GHz *Planck* bands. Bottom: comparison of the IR emission from this population of nanosilicates (red solid) to the observational constraints as in Figure 5.

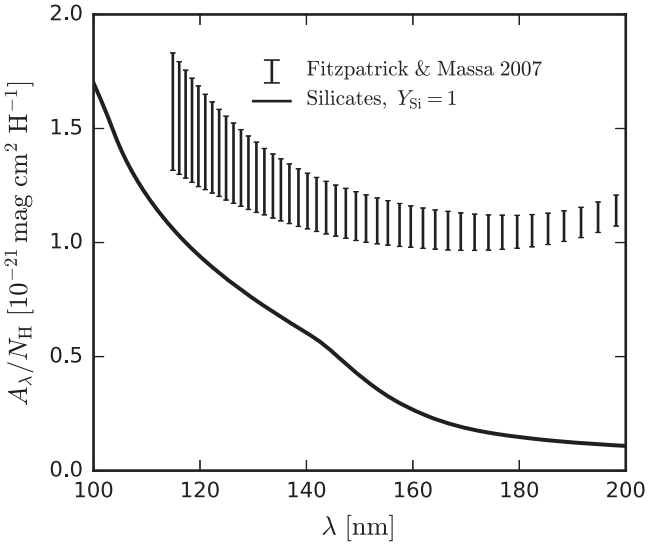

Figure 7. Comparison of the average interstellar extinction curve of Fitzpatrick & Massa (2007) to the extinction arising from a population of interstellar nanosilicates with $Y_{Si} = 1$. To normalize the extinction curve to the hydrogen column, we have taken $N_H/E(B-V) = 7.7 \times 10^{21}$ cm^{-2} mag^{-1} (Liszt 2014a, 2014b; Planck Collaboration et al. 2016b). Without assumptions on the extinction contributed by larger silicate grains and grains of other compositions, the UV extinction curve is unable to constrain the fraction of interstellar silicon in the form of nanosilicates.

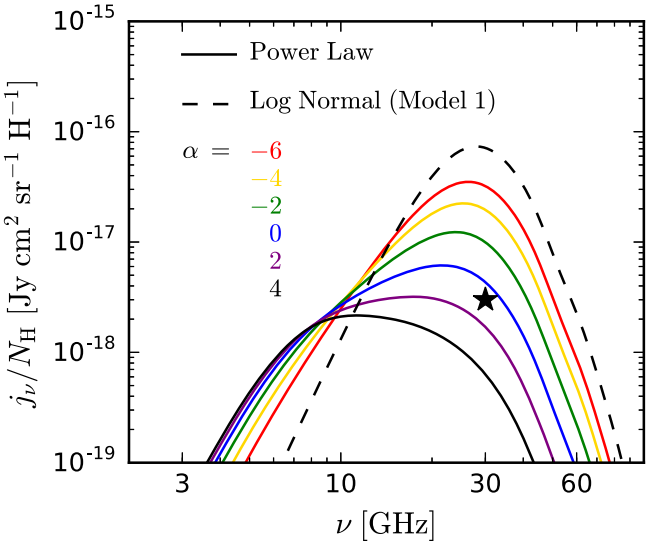

Figure 8. Spinning dust emission for silicate grains with $\beta = 0.3$ D having a lognormal size distribution (dashed line) and power-law size distributions (solid lines) assuming $Y_{Si} = 1$. For reference, the observed 30 GHz Galactic spinning dust emissivity of approximately 3×10^{-18} Jy sr^{-1} cm^2 H^{-1} is indicated with a star. As the power-law index α increases (i.e., as the size distribution is weighted toward larger grains), the spinning dust emissivity goes down and the peak frequency decreases. Further, as α increases, the slope of the 10–30 GHz portion of the SED becomes shallower. It is evident that the amplitude, shape, and peak frequency of the spinning dust SED are all sensitive to the shape of the grain size distribution.

6. A Generalized Model of Spinning Dust

We have demonstrated that the AME could arise from spinning nanoparticles of one or more different compositions, including PAHs, silicates, and metallic iron. The space of possible spinning dust SEDs is thus quite large, and it would be useful to articulate generalized, carrier-independent predictions that can test our theoretical understanding of spinning dust emission. In this section, we first highlight three major uncertainties in modeling spinning dust emission: the grain size distribution, the distribution of electric or magnetic dipole moments, and the grain charge distribution. We then discuss robust predictions from modeling in light of these uncertainties, with particular attention to extreme environments like PDRs. Finally, we suggest observational tests for identifying spinning dust emission with a particular carrier.

6.1. Model Uncertainties

6.1.1. Grain Size Distribution

Recognizing that the infrared dust emission features and the AME could potentially both be explained by a large population of ultrasmall carbonaceous grains (i.e., PAHs), Draine &

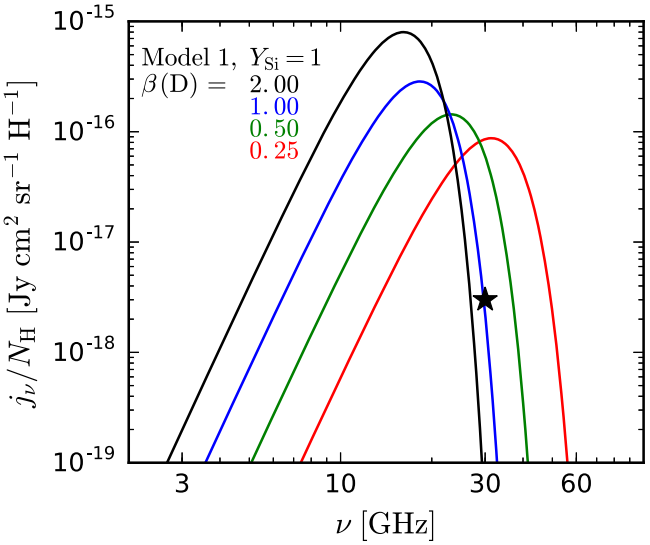

Figure 9. Spinning dust emission for silicate grains in which all grains are assumed to have a fixed dipole moment per atom β, i.e., there is no averaging over an electric dipole moment distribution. Both the spinning dust emissivity and peak frequency are strong functions of the electric dipole moment, rendering the spinning dust SED sensitive to the shape of the dipole moment distribution. For reference, the observed 30 GHz Galactic spinning dust emissivity of approximately 3×10^{-18} Jy sr^{-1} cm^2 H^{-1} is indicated with a star.

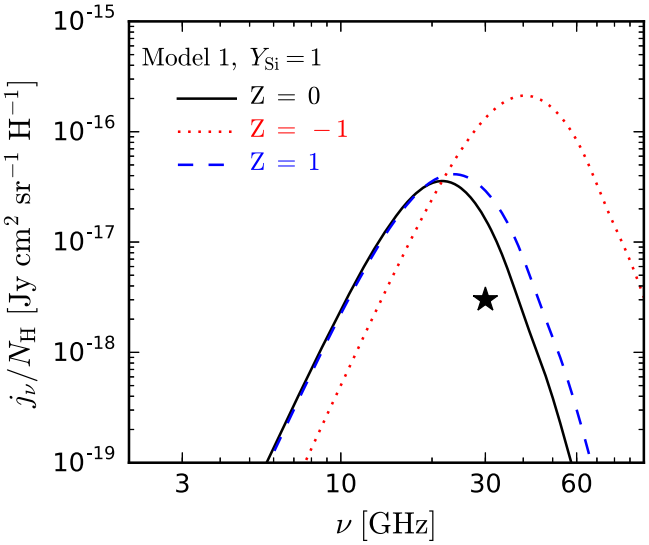

Figure 10. Spinning dust emission for silicate grains in which all grains are assumed to have a fixed charge Ze, i.e., there is no averaging over the charge distribution. While neutral and positively charged grains behave similarly, negatively charged grains are considerably more rotationally excited and have larger emissivities and higher peak frequencies. For reference, the observed 30 GHz Galactic spinning dust emissivity of approximately 3×10^{-18} Jy sr^{-1} cm^2 H^{-1} is indicated with a star.

Lazarian (1998b) proposed a lognormal component in the size distribution of carbonaceous grains peaked at a grain radius of 6 Å. Many subsequent studies have since adopted the lognormal parameterization of the size distribution (as we discuss in Section 2.3), which has also been the default in the `SpDust` code.

However, absent a detailed theory of dust formation and destruction, there is no particular reason why the size distribution of ultrasmall grains should be lognormal. Given the strong dependence of both the spinning dust emissivity and peak frequency on grain size (see Figure 1), we test the sensitivity of the spinning dust SED to the shape of the grain size distribution. Rather than a lognormal grain size distribution, we consider truncated power laws of the form

$$\frac{1}{n_H}\frac{dn}{da} = B\left(\frac{a}{a_{min}}\right)^{\alpha} \quad a_{min} \leqslant a \leqslant a_{max}, \tag{10}$$

where the normalization constant B is given by

$$B = \frac{3 m_X b_X}{4\pi\rho a_{min}^4} \times \begin{cases} \frac{4+\alpha}{-1+(a_{max}/a_{min})^{4+\alpha}} & \alpha \neq -4, \\ \frac{1}{\ln(a_{max}/a_{min})} & \alpha = -4. \end{cases} \tag{11}$$

Parameters m_X and b_X are as defined following Equation (9).

In Figure 8 we plot the spinning dust SED from silicate grains having electric dipole moment $\beta = 0.3$ D for different values of the power-law index α ranging from -6 to 4 and assuming $Y_{Si} = 1.0$, $a_{min} = 4.5$Å, $a_{max} = 10$ Å, and CNM conditions. For comparison, we also plot emission from the same silicate grains having a lognormal size distribution with $a_0 = a_{min} = 4.5$ Å and $\sigma = 0.1$ (i.e., model 1; see Equation (8)).

As the size distribution becomes weighted toward larger and larger grains (i.e., as α increases), the total spinning dust emissivity goes down and the peak frequency shifts to lower frequencies. It is also notable that the slope of the 10–30 GHz portion of the spinning dust SED becomes shallower as α increases, resulting in a less peaked spectrum. Further, in all cases, the slope of this portion of the SED differs from that of the lognormal distribution.

We therefore conclude that the spinning dust SED is quite sensitive to the shape of the grain size distribution, which can influence the shape, amplitude, and peak frequency of the SED even when all other parameters are held fixed. As the AME SED becomes better determined observationally, its "peakiness" may provide constraints on the grain size distribution.

6.1.2. Dipole Moment Distribution

The electric dipole moment of a PAH or silicate grain of N_{at} atoms has been modeled as a "random walk" process, with each atom contributing an electric dipole moment β in a random direction. This leads to a Gaussian distribution of electric dipole moments with variance proportional to N_{at}. How sensitive is the resulting spinning dust SED to the form of this distribution?

Ali-Haïmoud et al. (2009) demonstrated that, for a PAH of radius 3.5 Å, the peak frequency of emission could vary from about 30 GHz for grains with electric dipole moments twice the rms value to over 100 GHz for grains with electric dipole moments less than 3% of the rms value (see their Figure 10). This occurs because the electric dipole radiation provides much of the rotational damping for $\beta > 0.3$ D. Further, they found the total radiated power to increase with increasing electric dipole moment.

In Figure 9 we perform a similar analysis for silicate grains. Assuming a lognormal size distribution with $a_0 = a_{min} = 4.5$ Å and $\sigma = 0.1$ (i.e., model 1), $Y_{Si} = 1$, and CNM conditions, we fix the intrinsic electric dipole moment for all grains with N_{at} atoms to the value $\mu_i = \beta\sqrt{N_{at}}$ for different values of β. The trends observed for PAHs are evident here–increasing β lowers the peak frequency and increases the

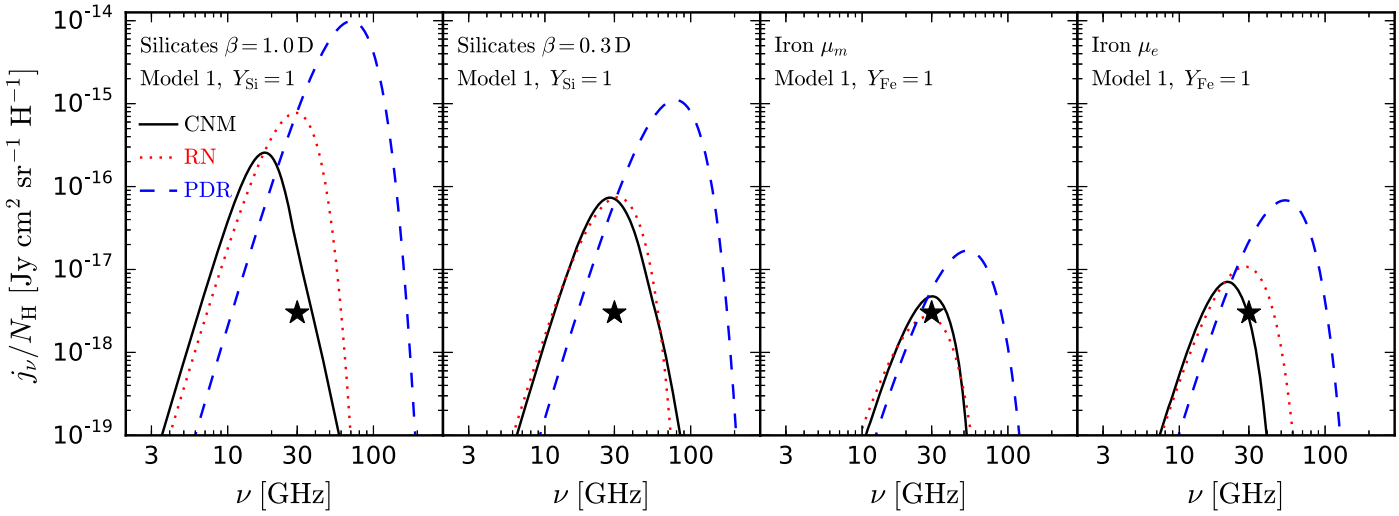

Figure 11. Spinning dust emission for silicate and iron grains in CNM, RN, and PDR environments.

emissivity. The spinning dust SED averaged over electric dipole moments must then depend on the relative weighting of grains with large dipole moments that are highly emissive at relatively low frequencies and grains with small dipole moments that radiate predominantly at higher frequencies.

6.1.3. Grain Charge Distribution

A third distribution that must be considered is the grain charge distribution, as many excitation and damping mechanisms, such as collisions with ions, depend strongly on the grain charge. Detailed models of grain charging in various interstellar environments have been presented in the literature (Draine & Sutin 1987; Bakes & Tielens 1994; Weingartner & Draine 2001b; Hensley & Draine 2017), though it should be kept in mind that these models are often limited by available laboratory data for the materials of interest and thus come with some uncertainty. This uncertainty is exacerbated by the difficulty of constraining the grain charge distribution observationally.

To assess the influence of grain charge on the spinning dust SED, in Figure 10 we plot the SEDs of a population of silicate grains with a lognormal size distribution with $a_0 = a_{\rm min} = 4.5$ Å, $\sigma = 0.1$ (i.e., model 1), $Y_{\rm Si} = 1$, and $\beta = 0.3$ D assuming CNM conditions and that all grains have charge of -1, 0, or 1. The SEDs of the positively charged and neutral grains are quite similar, but the negatively charged grains are significantly more rotationally excited, having both a higher peak frequency and higher emissivity. Particularly in a low-temperature environment like the CNM, the dominant rotational excitation mechanism is collisions with gas atoms and ions, with ion collisions being particularly important for negatively charged grains. Due to Coulomb attraction, negatively charged grains have a much higher collisional cross section with positive ions than neutral grains and thus have a rotational excitation coefficient G_i (see Draine & Lazarian 1998b, Equation (39)) more than a factor of 20 larger.

Weingartner & Draine (2001b) found that of order 10% of both PAHs and ultrasmall silicates are negatively charged in CNM and WNM conditions, and Hensley & Draine (2017) found that roughly 20% and 50% of metallic iron nanoparticles are negatively charged in the CNM and WNM, respectively. These calculations suggest that negatively charged grains constitute a non-negligible fraction of interstellar nanoparticles and their abundance could strongly influence the shape of the spinning dust spectrum.

6.1.4. Highly Irradiated Environments

In the CNM, WNM, and WIM environments we have considered thus far, we have assumed that the radiation field is identical to the interstellar radiation field measured by Mathis et al. (1983). In this section, we consider the more highly irradiated environments of RNs and PDRs, where the radiation field is assumed to be a factor $\chi = 10^3$ and 10^5 times more intense, respectively (see Table 1).

Ali-Haïmoud et al. (2009) demonstrated that the spinning dust emission spectrum from PAHs in CNM conditions was relatively unaffected by the strength of the radiation field from $10^{-2} \lesssim \chi \lesssim 10^2$ in either peak emissivity or peak frequency. However, for $\chi \gtrsim 10^2$, rotational excitation from photon emission becomes important relative to other excitation mechanisms, and both the peak emissivity and peak frequency begin to increase with increasing radiation field strength. In the Table 1 RN environment, rotational excitation of PAHs is indeed dominated by IR emission, though collisional excitation is dominant in PDRs (see Ali-Haïmoud 2013, Table 1).

Figure 11 illustrates the emission spectra from silicates and iron grains in CNM, RN, and PDR environments. For silicates with $\beta = 1.0$ D, the spectrum shifts to higher peak frequency and peak emissivity moving from CNM to RN to PDR environments, much as has been observed for PAHs. However, for silicates with $\beta = 0.3$ D, the CNM and RN spectra are remarkably similar.

Due to the strong radiation field, rotational damping due to the thermal emission of IR photons is the dominant damping mechanism in the RN environment. In contrast, rotational damping from rotational electric dipole emission dominates in the CNM. Thus, the peak frequency of the AME spectrum is sensitive to the value of β in the CNM but loses much of that sensitivity in the case of RN.

In PDRs, collision with neutrals is by far the dominant excitation mechanism owing to the high density of these regions, and the peak emissivity and peak frequency of the spinning dust emission spectrum are accordingly high relative to other environments.

The iron grains tell a similar story—the enhanced radiation field in an RN makes little difference to the rotational emission, but the enhanced gas density of PDRs shifts the spectrum to both higher emissivity and peak frequency.

6.2. Generic Predictions of Spinning Dust Theory

Spinning dust emission, which may constitute all or part of the observed AME, could arise from several distinct populations of nanoparticles, each with their own size, charge, and dipole moment distributions. Further, particularly in low-resolution CMB experiments, the emission may be arising from multiple distinct interstellar environments. All of these factors make predicting the expected spinning dust spectrum exceedingly difficult. Therefore, fits to a single AME SED may not be terribly informative as to either the conditions of the interstellar environment from which the emission originates or the nature of the dust grains doing the emitting. In light of this, we suggest a way forward for testing and improving our theoretical understanding of spinning dust emission by performing observational tests on the *relative* emission spectra of various environments.

Regardless of the type of nanoparticle producing the rotational emission, the spinning dust SED is highly sensitive to the abundance of the very smallest grains. In particularly dense environments where small grains are expected to be heavily depleted by coagulation, the spinning dust emissivity per total dust mass (or dust luminosity) should be substantially smaller than in lower-density clouds or the diffuse ISM. Tibbs et al. (2016) have presented initial evidence of this through nondetection of AME in dense Galactic cores. Measurements of the AME emissivity as a function of the local gas density should reveal a steady decline in 30 GHz emissivity with increasing gas density.

A second carrier-independent feature of spinning dust emission is the importance of ion collisions as a rotational excitation mechanism, particularly for negatively charged grains. In environments where there is an observable change in the ionization fraction of the gas, such as within a PDR, one may expect a corresponding shift in the spinning dust emission to higher emissivities and higher peak frequencies as the gas becomes more ionized. Note that in photoionized H II gas, the increased electron density can result in an increased fraction of negatively charged nanoparticles with increased rotational excitation by ion collisions.

In addition to Galactic cores and PDRs, external galaxies provide an excellent testbed for statistical study of the dependence of the AME spectra with environmental conditions. The inherent faintness of the AME signal makes such measurements challenging, but a campaign targeting nearby galaxies with ample ancillary measurements at other wavelengths would likely yield invaluable insight into the environmental factors influencing the AME spectrum and provide tests of the current formulation of spinning dust theory.

Finally, as new data sets such as C-BASS (King et al. 2014) come online and component separation algorithms continue to improve, further analysis of this type will be made possible on the AME originating in the diffuse Galactic ISM.

6.3. Identifying the Carrier(s) of Spinning Dust Emission

Having discussed the generic predictions of spinning dust emission arising from a nanoparticle of arbitrary composition, we now turn to ways to identify the particles responsible for the emission. Once again, we argue that it is difficult to extract information from the spinning dust SED itself, and therefore we turn to correlations between the spinning dust SED and other tracers of ultrasmall grains.

A first test of this type has been tests of the association of the infrared emission features with the AME, though no compelling correlation has been found to date (Tibbs et al. 2011, 2012; Vidal et al. 2011; Hensley et al. 2015, 2016). These studies strongly suggest that the AME does not originate primarily from the PAH population.

Silicate and metallic iron nanoparticles do not have such striking emission features, but similar tests may be possible. For instance, if ultrasmall silicates are able to produce significant 10 μm emission, then there may be observable correlation between this emission and the AME. However, such measurements will be challenging, due to the difficulty of distinguishing the silicate contribution near 10 μm from the wings of the PAH features at 8.6 and 11.2 μm.

Very small free-flying Fe nanoparticles become very cold between photon absorptions and emit relatively little thermal power at FIR and millimeter wavelengths. However, if Fe nanoparticles are also present as inclusions, or if the free-flier population includes Fe nanoparticles with sizes $a > 10$ Å, the thermal magnetic dipole emission can result in spectral flattening of the dust SED at long wavelengths and a corresponding drop in the polarization fraction of the thermal dust emission (Draine & Hensley 2013). Such signatures could be correlated with the AME.

Iron nanoparticles may also emit strongly near 20 μm (see Figure 5). If the Fe nanoparticles are partially oxidized, energy may be radiated in vibrational modes (e.g., 22 μm FeO, 16.4 μm Fe_3O_4). Assessing the correlation between the short-wavelength dust emission and the AME will be valuable if systematic trends do exist, though it will be difficult to interpret in terms of a specific carrier.

7. Discussion

Despite the historical association of spinning dust emission with PAHs, we demonstrate, in qualitative agreement with Hoang & Lazarian (2016) and Hoang et al. (2016), that spinning nanoparticles of other compositions can compose a portion, or even the entirety, of the observed AME. We demonstrate that variations in the assumed distributions of grain properties, such as size, charge, and dipole moments, can lead to large changes in the spinning dust SED. This suggests that the model space is rich enough to accommodate the observed diversity in AME SEDs.

However, even the generalized spinning dust hypothesis is not without its problems. Hensley et al. (2016) defined a parameter $f_{\rm PAH}$, based on the ratio of the 12 μm intensity to the total dust radiance, as an indicator of the PAH abundance per dust mass. They found evidence that this parameter evolved systematically with both the dust radiance and the dust optical depth, with lower values of $f_{\rm PAH}$ observed in regions with less dust. This could be due to an increase in PAH destruction and/or a decrease in PAH formation in low-density regions. Indeed, Sandstrom et al. (2010) found that the PAH abundance in the Small Magellanic Cloud is highest near molecular clouds, suggesting that PAH formation occurs primarily in the denser regions and PAH destruction takes place in the more diffuse regions. Ultrasmall grains of other compositions are also

expected to be more susceptible to destruction in these conditions (Guhathakurta & Draine 1989), making $f_{\rm PAH}$ a seemingly reasonable proxy for the abundance of all ultrasmall grains irrespective of composition.

Insofar as this is the case, the empirical results of Hensley et al. (2016)—that the AME emissivity per dust radiance shows no evidence of variation with changes in environmental conditions—seem to argue *against* the spinning dust paradigm in general, as spinning dust emission arises preferentially from the very smallest grains (see Figure 1). It is possible, however, that the destruction and formation mechanisms for PAHs are sufficiently different processes from those of other grain types that the populations do not vary in tandem. Complementary tests of the link between the AME and the abundance of ultrasmall grains of the kind suggested in Section 6.2 are greatly needed.

A second challenge to the spinning dust paradigm is the apparent positive correlation between the strength of the AME and the strength of the radiation field (Tibbs et al. 2011, 2012; Planck Collaboration et al. 2014c; Hensley et al. 2016). Theoretically, one expects the radiation field itself to have only minor effects on the rotational emission in most environments. Indeed, the radiation field serves mostly to heat grains to higher temperatures and thereby increase the amount of rotational damping due to infrared emission (Draine & Lazarian 1998b; Ali-Haïmoud et al. 2009; Ysard & Verstraete 2010).

However, the strength of the radiation field is also correlated with other environmental parameters, such as the gas density and ionization state, that are important for the rotational excitation of ultrasmall grains. Further, regions with a higher radiation field likely have more star formation, more diffuse molecular clouds, and perhaps more production of nanoparticles via fragmentation. Finally, strong radiation fields may affect the abundance of the smallest grains through enhanced sublimation. Self-consistent ISM models, such as those constructed by Ysard et al. (2011), may be helpful in assessing whether the correlation between the AME and the radiation field can be reproduced within the spinning dust paradigm.

8. Conclusion

The principal conclusions of this work are as follows:

1. Nanosilicates are viable carriers of the AME if a small fraction of the interstellar silicon ($Y_{\rm Si} \sim 0.04$–0.14 for models 1 and 2 with $\beta = 0.3$ D) is in the form of ultrasmall grains, in agreement with similar calculations by Hoang et al. (2016). We further demonstrate that the entirety of the AME signal inferred from *Planck* and *WMAP* observations can be accounted for by nanosilicates without violating observational constraints on mid-infrared emission or ultraviolet extinction. In Figure 6 we present a specific model where the AME SED is reproduced with $Y_{\rm Si} = 0.06$.
2. Iron nanoparticles are capable of producing some of the observed AME, as found by Hoang & Lazarian (2016), but cannot reproduce it in its entirety without violating constraints on the interstellar iron abundance and/or the mid-infrared emission. The infrared emission following single-photon heating strongly constrains the abundance of Fe nanoparticles.
3. The spinning dust SED is highly sensitive to the grain size distribution, charge distribution, and dipole moment distribution, making direct inferences from the SED alone challenging.
4. Observations constraining the variations of the AME spectrum with environment, in particular the peak frequency and emissivity per dust column, can provide critical tests of the spinning dust hypothesis and help elucidate the nature of the AME carrier(s). Variations in the AME spectrum as a function of local density and depth into a PDR may be especially informative.
5. Some shortcomings of the spinning PAH hypothesis, such as the observed link between the AME and the strength of the radiation field and the noncorrelation of the AME with the PAH abundance, also pose problems for spinning non-PAHs. More tests of the spinning dust paradigm are needed.

We thank the organizers and participants of the 2016 AME Workshop at ESTEC for many stimulating conversations that informed this work and the anonymous referee for helpful comments. B.T.D. acknowledges support from NSF grant AST-1408723. The research was carried out in part at the Jet Propulsion Laboratory, California Institute of Technology, under a contract with the National Aeronautics and Space Administration.

References

Ali-Haïmoud, Y. 2013, AdAst, 2013, 462697
Ali-Haïmoud, Y., Hirata, C. M., & Dickinson, C. 2009, MNRAS, 395, 1055
Allamandola, L. J., Tielens, A. G. G. M., & Barker, J. R. 1985, ApJL, 290, L25
Allamandola, L. J., Tielens, A. G. G. M., & Barker, J. R. 1989, ApJS, 71, 733
Altobelli, N., Postberg, F., Fiege, K., et al. 2016, Sci, 352, 312
Asplund, M., Grevesse, N., Sauval, A. J., & Scott, P. 2009, ARA&A, 47, 481
Bakes, E. L. O., & Tielens, A. G. G. M. 1994, ApJ, 427, 822
Battistelli, E. S., Carretti, E., Cruciani, A., et al. 2015, ApJ, 801, 111
Bensby, T., Feltzing, S., Lundström, I., & Ilyin, I. 2005, A&A, 433, 185
Billas, I. M. L., Becker, J. A., Châtelain, A., & de Heer, W. A. 1993, PhRvL, 71, 4067
Bradley, J. P. 1994, Sci, 265, 925
Brown, M. J. I., Moustakas, J., Smith, J.-D. T., et al. 2014, ApJS, 212, 18
Chiappini, C., Romano, D., & Matteucci, F. 2003, MNRAS, 339, 63
Dobler, G., Draine, B., & Finkbeiner, D. P. 2009, ApJ, 699, 1374
Dobler, G., & Finkbeiner, D. P. 2008, ApJ, 680, 1222
Draine, B. T., & Hensley, B. 2013, ApJ, 765, 159
Draine, B. T., & Hensley, B. S. 2016, ApJ, 831, 59
Draine, B. T., & Lazarian, A. 1998a, ApJL, 494, L19
Draine, B. T., & Lazarian, A. 1998b, ApJ, 508, 157
Draine, B. T., & Li, A. 2001, ApJ, 551, 807
Draine, B. T., & Li, A. 2007, ApJ, 657, 810
Draine, B. T., & Sutin, B. 1987, ApJ, 320, 803
Dwek, E., Arendt, R. G., Fixsen, D. J., et al. 1997, ApJ, 475, 565
Fitzpatrick, E. L., & Massa, D. 2007, ApJ, 663, 320
Génova-Santos, R., Martín, J. A. R., Rebolo, R., et al. 2015, MNRAS, 452, 4169
Guhathakurta, P., & Draine, B. T. 1989, ApJ, 345, 230
Hensley, B., Murphy, E., & Staguhn, J. 2015, MNRAS, 449, 809
Hensley, B. S., & Draine, B. T. 2017, ApJ, 834, 134
Hensley, B. S., Draine, B. T., & Meisner, A. M. 2016, ApJ, 827, 45
Hoang, T., Draine, B. T., & Lazarian, A. 2010, ApJ, 715, 1462
Hoang, T., & Lazarian, A. 2016, ApJ, 821, 91
Hoang, T., Lazarian, A., & Draine, B. T. 2011, ApJ, 741, 87
Hoang, T., Vinh, N.-A., & Quynh Lan, N. 2016, ApJ, 824, 18
Ingalls, J. G., Bania, T. M., Boulanger, F., et al. 2011, ApJ, 743, 174
Jenkins, E. B. 2009, ApJ, 700, 1299
Keller, L. P., & McKay, D. S. 1997, GeCoA, 61, 2331
King, O. G., Jones, M. E., Blackhurst, E. J., et al. 2014, MNRAS, 438, 2426
Leger, A., & Puget, J. L. 1984, A&A, 137, L5
Li, A., & Draine, B. T. 2001, ApJL, 550, L213
Liszt, H. 2014a, ApJ, 783, 17
Liszt, H. 2014b, ApJ, 780, 10
Lodders, K., Palme, H., & Gail, H.-P. 2009, LanB, 4, 44

Mathis, J. S., Mezger, P. G., & Panagia, N. 1983, A&A, 128, 212
Miville-Deschênes, M.-A., Ysard, N., Lavabre, A., et al. 2008, A&A, 490, 1093
Onaka, T., Yamamura, I., Tanabe, T., Roellig, T. L., & Yuen, L. 1996, PASJ, 48, L59
Planck Collaboration, Abergel, A., Ade, P. A. R., et al. 2014a, A&A, 571, A11
Planck Collaboration, Abergel, A., Ade, P. A. R., et al. 2014b, A&A, 566, A55
Planck Collaboration, Adam, R., Ade, P. A. R., et al. 2016a, A&A, 594, A10
Planck Collaboration, Ade, P. A. R., Aghanim, N., et al. 2014c, A&A, 565, A103
Planck Collaboration, Ade, P. A. R., Aghanim, N., et al. 2016b, A&A, 586, A132
Planck Collaboration, Ade, P. A. R., Aghanim, N., et al. 2016c, A&A, 594, A25
Poteet, C. A., Whittet, D. C. B., & Draine, B. T. 2015, ApJ, 801, 110
Remazeilles, M., Dickinson, C., Eriksen, H. K. K., & Wehus, I. K. 2016, MNRAS, 458, 2032
Sandstrom, K. M., Bolatto, A. D., Draine, B. T., Bot, C., & Stanimirović, S. 2010, ApJ, 715, 701
Silsbee, K., Ali-Haïmoud, Y., & Hirata, C. M. 2011, MNRAS, 411, 2750
Smith, J. D. T., Draine, B. T., Dale, D. A., et al. 2007, ApJ, 656, 770
Tiago, M. L., Zhou, Y., Alemany, M. M. G., Saad, Y., & Chelikowsky, J. R. 2006, PhRvL, 97, 147201
Tibbs, C. T., Flagey, N., Paladini, R., et al. 2011, MNRAS, 418, 1889
Tibbs, C. T., Paladini, R., Cleary, K., et al. 2016, MNRAS, 456, 2290
Tibbs, C. T., Paladini, R., Compiègne, M., et al. 2012, ApJ, 754, 94
Tibbs, C. T., Watson, R. A., Dickinson, C., et al. 2010, MNRAS, 402, 1969
van Hoof, P. A. M., Weingartner, J. C., Martin, P. G., Volk, K., & Ferland, G. J. 2004, MNRAS, 350, 1330
Vidal, M., Casassus, S., Dickinson, C., et al. 2011, MNRAS, 414, 2424
Weingartner, J. C., & Draine, B. T. 2001a, ApJ, 548, 296
Weingartner, J. C., & Draine, B. T. 2001b, ApJS, 134, 263
Westphal, A. J., Stroud, R. M., Bechtel, H. A., et al. 2014, Sci, 345, 786
Ysard, N., Juvela, M., & Verstraete, L. 2011, A&A, 535, A89
Ysard, N., Miville-Deschênes, M. A., & Verstraete, L. 2010, A&A, 509, L1
Ysard, N., & Verstraete, L. 2010, A&A, 509, A12